Available online at www.sciencedirect.com
ScienceDirect
Trans. Nonferrous Met. Soc. China 35(2025) 2021−2035
Transactions of Nonferrous Metals Society of China
www.tnmsc.cn

Mechanical performance of hard red sandstone in acoustic emission integrated conventional triaxial compression tests

Kun DU[1], Ming-hui LIU[1], Xue-feng LI[1], Li-chang WANG[2], Jian ZHOU[1], Tao YANG[3], Peng LI[4]

1. School of Resources and Safety Engineering, Central South University, Changsha 410083, China;
2. School of Geosciences and Info-physics, Central South University, Changsha 410083, China;
3. School of Mine Safety, North China Institute of Science and Technology, Langfang 065201, China;
4. Zhongnan Engineering Corporation Limited, Changsha 410014, China

Received 21 November 2023; accepted 26 August 2024

Abstract: A series of acoustic emission (AE)-integrated conventional triaxial compression tests (CTTs) were conducted to evaluate the mechanical properties of hard red sandstone. Under conventional triaxial stress states, the crack closure stress, crack initiation stress, and damage stress ranged in 13.75%−22.34%, 31.84%−42.19%, and 63.85%−75.93% of the peak strength of sandstone, respectively. The AE parameters reflected the confining pressure (σ_3) effect on microcrack propagation, with σ_3=5 MPa identified as the threshold affecting both the timing of numerous AE hits and the distribution range of peak frequencies of AE signals before the final failure of each specimen. The AE property analysis showed that shear cracks played a dominant role in rock failure in CCTs, which ranged in 60%−85% of the total number of cracks. A smaller σ_3 value promoted shear failure, whereas a larger σ_3 value inhibited it. Furthermore, the appropriate dataset selection range to accurately calculate the cohesion force and internal friction angle in CTTs and variable-angle shear tests was determined.

Key words: red sandstone; mechanical parameters; stress threshold, acoustic emission characteristics; internal friction angle; cohesion force

1 Introduction

As a typical sedimentary rock, sandstone is a widely encountered natural material on both the surface and underground [1−3], such as high-steep slopes [4] and underground tunnels [5]. However, the lack of comprehensive research on the mechanical and failure characteristics of sandstone has resulted in a dearth of effective control measures for engineering projects involving this material. Consequently, various geological disasters have occurred [6,7], posing severe risks to construction personnel and causing substantial economic losses. Thus, analyzing the mechanical properties and failure characteristics of sandstone through laboratory tests could provide insights into the mechanisms of rock engineering disasters.

It is often assumed that sandstone is subjected to conventional triaxial stress, that is, σ_1(maximum principal stress, i.e. peak stress) > σ_2(intermediate principal stress) = σ_3(minimum principal stress, confining pressure), particularly in underground gas and oil storage projects. Consequently, researchers have conducted laboratory tests and numerical simulations to analyze the mechanical and failure characteristics of sandstone under such stress conditions. Researchers have investigated trends in residual strength [8], permeability [9,10], seismic source characteristics [11], porosity [12,13], and geological structure formation [14] with increasing the confining pressure. Moreover, in engineering

Corresponding author: Li-chang WANG, Tel: +86-15116433704, E-mail: wlccsu@csu.edu.cn
https://doi.org/10.1016/S1003-6326(25)66798-7

applications, the influence of environmental factors such as water and temperature, mineral composition, and internal structure on the mechanical properties of sandstone cannot be overlooked [15−19].

Numerous laboratory studies have demonstrated the close relationship between rock strength and initiation of microcracks during loading [20,21]. Understanding the stress thresholds of rocks is essential to accurately evaluate the damage evolution process from a microscopic perspective [22]. These stress thresholds, from the beginning of loading to the final failure of the rock, include the crack closure stress (σ_{cc}), crack initiation stress (σ_{ci}), damage stress (σ_{cd}), and peak strength (σ_{max}). Acoustic emission (AE) detection technology is a nondestructive method that is widely used in laboratory experiments to characterize rock failure behavior [23−25]. AE monitoring systems are often employed as auxiliary tools to detect microcrack activity in sandstone under various stress conditions, thereby facilitating the study of failure mechanisms. For example, through AE monitoring, changes in AE parameters have been used to effectively depict the failure modes of sandstone in compression–shear coupled stress states [26,27] and under biaxial fatigue stress conditions [28]. Furthermore, the time–frequency characteristics of signals provide valuable insights into the microcrack propagation and evolution processes in sandstone [29,30]. However, existing research has primarily focused on failure features in specific uniaxial stress states, making it difficult to detect the AE signals of rocks under triaxial stress conditions.

Therefore, in this study, a series of AE-integrated conventional triaxial compression tests (AE-CTTs) were conducted under varying confining pressures to comprehensively study the mechanical and failure characteristics of hard red sandstone. In addition, uniaxial compression tests (UCTs) and variable-angle shear tests (VASTs) were conducted to compare the difference in the mechanical performances of red sandstone under different stress states. The findings of this study can provide valuable insights for the safe design and construction of rock engineering projects.

2 Experimental

2.1 Test apparatus

An MTS-815 electrohydraulic servo testing system, with a maximum triaxial load, maximum confining pressure, and loading precision of 2600 kN, 140 MPa, and ±0.5%, respectively, was used, and a photograph of the system is shown in Fig. 1(a). In addition, a PCI-2 AE system was used to collect AE signals during the failure process of red sandstone. A conventional triaxial testing fixture equipped with specialized RT100 AE sensors was used (Figs. 1(b, c)). AE sensors were in direct contact with the surfaces of rock specimens. AE preamplifiers, sampling threshold, sampling rate, and sampling length were set to be 40 dB, 40 dB, 10 MSPS, and 10k, respectively.

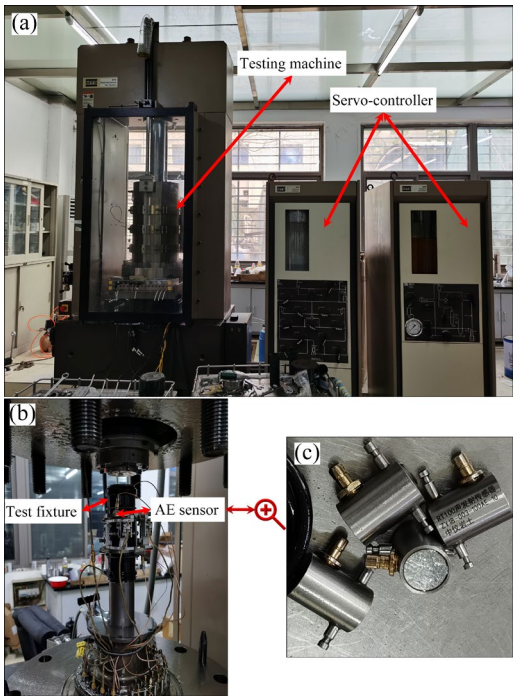

Fig. 1 Photographs of MTS-815 test system: (a) Overview of testing system; (b) Test fixture; (c) RT100 AE sensors

2.2 Specimen preparation

Cylindrical red sandstone specimens with a diameter of 50 mm and a height of 100 mm were prepared, as illustrated in Fig. 2(a). To minimize the influence of irrelevant variables, all rock specimens were drilled from the same rock mass and polished carefully to ensure that non-parallelism and non-perpendicularity were less than 0.2 mm, in accordance with the International Society for Rock Mechanics (ISRM) standards [31]. All specimens maintained good integrity and homogeneity.

The AE sensors were installed at fixed positions owing to the limitations of a conventional triaxial testing fixture. In the CTTs, near the upper and lower ends of the rock specimen, four AE sensors were symmetrically mounted, as shown in

Figs. 2(b, c). Before loading, each AE sensor was checked using a broken lead test. To ensure that the AE sensors closely adhered to the surface of the rock specimen and expelled any air, a film of a coupling agent was placed on the contact surface between the sensor and the rock specimen. A ring iron washer and a custom AE sensor fixture were used to secure the AE sensor close to the surface of the rock specimen during loading.

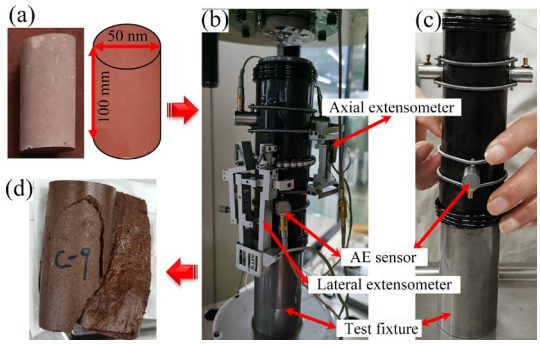

Fig. 2 Photographs of CTT fixture device and specimen: (a) Red sandstone specimen; (b) Conventional triaxial fixture; (c) Installation fixture for AE sensors; (d) Failed rock specimen

2.3 Experimental scheme

Before loading, petroleum jelly was applied to the surfaces of the rock specimens in contact with the loading blocks as antifriction treatment to reduce the influence of friction and the end effect on the results. The loading mode was selected as the displacement control mode with a loading rate of 0.10 mm/min. To determine the mechanical properties of the rock, such as the elastic modulus E and Poisson's ratio v, three extensometers (two axial and one radial) were set up in CTTs. To measure the basic parameters of sandstone more accurately, CTTs were conducted under confining pressures of 0, 2, 5, 8, 10, 12, 15, and 20 MPa, based on the in-situ stress distribution of underground engineering within a depth range of 50−800 m [32]. In addition, the tests were repeated 2−5 times under the same stress conditions to minimize accidental errors.

3 Results and analysis

3.1 Shear strength parameters in CTTs

3.1.1 Evaluation method

CTTs were used to measure the cohesive force (c) and the internal friction angle (φ) of sandstone through the common tangent drawing method. The specific calculation method is as follows: assuming that number of CTTs (n) under different confining pressures have been completed, the maximum principal stress and minimum principal stress of the ith test are σ_{1i} and σ_{3i}, respectively. The following formula can be obtained based on the Mohr–Coulomb criterion:

$$\frac{1}{2}(\sigma_{1i}-\sigma_{3i})=c\cos\varphi+\frac{1}{2}(\sigma_{1i}+\sigma_{3i})\sin\varphi \tag{1}$$

Let,

$$y_i=\frac{1}{2}(\sigma_{1i}-\sigma_{3i}),\ x_i=\frac{1}{2}(\sigma_{1i}+\sigma_{3i}) \tag{2}$$

Equation (1) can be expressed as follows:

$$y_i=c\cos\varphi+x_i\sin\varphi \tag{3}$$

The square of the deviation can be used to describe the degree of deviation as follows:

$$Q(c,\varphi)=\sum_{i=1}^{n}(y_i-c\cos\varphi-x_i\sin\varphi)^2 \tag{4}$$

where $Q(c, \varphi)$ is the non-negative quadratic function of c and φ; therefore, its minimum value exists and is equal to the sum of the squares of the distance between the shear strength envelope obtained by linear regression and the tangent point of the Mohr stress circle. If $Q(c, \varphi)=0$, the shear strength envelope is exactly tangent to Mohr stress circles. Because the actual shear strength envelope is not tangential to Mohr circles obtained in all the tests, the following equations can be derived using the principle of minimum value:

$$\begin{cases}\dfrac{\partial Q}{\partial c}=-2\sum_{i=1}^{n}(y_i-c\cos\varphi-x_i\sin\varphi)\times(-\cos\varphi)=0\\ \dfrac{\partial Q}{\partial \varphi}=-2\sum_{i=1}^{n}(y_i-c\cos\varphi-x_i\sin\varphi)\times\\ \qquad(c\sin\varphi-x_i\cos\varphi)=0\end{cases} \tag{5}$$

By solving Eq. (5), we can obtain

$$\varphi=\arcsin\left(\frac{\sum_{i=1}^{n}x_iy_i-\bar{x}\sum_{i=1}^{n}y_i}{\sum_{i=1}^{n}x_i^2-\bar{x}\sum_{i=1}^{n}x_i}\right)\quad c=\frac{\bar{y}}{\cos\varphi}-\bar{x}\tan\varphi \tag{6}$$

where

$$\begin{cases}\overline{x}=\dfrac{1}{n}\sum_{i=1}^{n}x_i\\ \overline{y}=\dfrac{1}{n}\sum_{i=1}^{n}y_i\end{cases} \tag{7}$$

In a rectangular coordinate system, Mohr stress circles under various confining pressures can be drawn with the normal stress σ as the abscissa and the shear stress τ as the ordinate. The center of each circle is at $(\sigma_1+\sigma_3)/2$ and the radius is $(\sigma_1-\sigma_3)/2$. Equations (1)−(7) can be used to compute the common tangents of Mohr stress circles. The sum of the squares of the distances between the common tangent and all tangent points of Mohr stress circles is minimized. This common tangent is the shear strength line, the intercept of the common tangent on the ordinate axis is c, and the angle between the common tangent and the abscissa axis is φ.

3.1.2 Effect of σ_3 on mechanical properties

Based on the results of the peak strength σ_{max} under different confining pressures σ_3 in the CTTs, the c and φ values of red sandstone were 25.59 MPa and 45.29°, respectively. The results of CTTs and UCTs are presented in Table 1 and Figs. 3 and 4. It should be noted that the results presented in Table 1 are the average values of repeated tests.

Table 1 Mechanical properties of red sandstone in different CTTs

σ_3/MPa	σ_{max}/MPa	E/GPa	v
0	117.39	22.46	0.212
2	132.63	23.16	0.205
5	157.90	24.28	0.189
8	182.64	26.84	0.169
10	190.44	26.35	0.179
12	195.47	26.16	0.151
15	213.08	26.61	0.172
20	231.52	26.22	0.159

The measured E and v values of red sandstone under uniaxial stress were 22.46 GPa and 0.212, respectively. However, for deep-buried projects with high in situ stress, σ_3 to be loaded in the test should be selected according to the level of in situ stress. Figure 4 shows that the peak strength continues to increase as σ_3 increases, and the upward trend resembles a parabolic curve. The

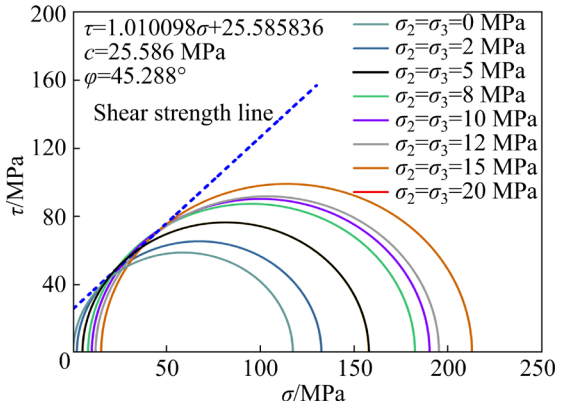

Fig. 3 Mohr stress circles and shear strength line

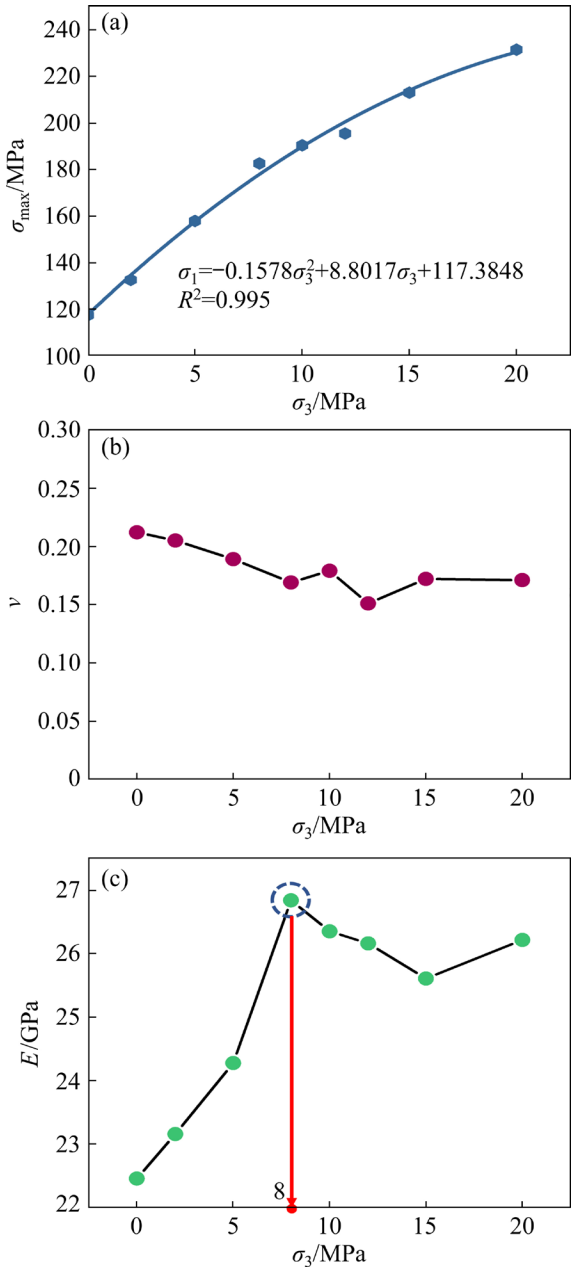

Fig. 4 Effects of σ_3 on peak stress (a), Poisson's ratio (b), and elastic modulus (c)

Poisson's ratio ν of sandstone initially decreased and then slightly increased with an increase in σ_3, reaching its minimum value at σ_3=12 MPa. This indicated that confining pressure could restrain the radial deformation of sandstone, but excessive σ_3 would inhibit axial deformation. The elastic modulus E of sandstone initially increased rapidly with an increase in σ_3, reaching its maximum value at σ_3=8 MPa, and then decreased. When the σ_3 value was small, even slight changes in σ_3 exerted a disproportionately significant influence on the deformation properties of red sandstone. These findings suggest that, in shallow-buried underground engineering projects with low in-situ stress, it is crucial to consider the influence of σ_3 on the properties of the rock mass. Furthermore, different design reference parameters should be selected based on the varying confining pressures and in-situ stresses.

3.2 Stress thresholds in CTTs

The strength behavior of rock can be evaluated based on four types of stress thresholds, that is, the crack closure stress (σ_{cc}), crack initiation stress (σ_{ci}), damage stress (σ_{cd}), and peak strength (σ_{max}) [22]. The stress–strain curves measured in CTTs and the corresponding four types of stress thresholds during the loading process of each rock specimen are shown in Fig. 5.

According to the calculation method described by NICKSIAR and MARTIN [33], the stress thresholds under different σ_3 values were calculated. The red dashed line in Fig. 5 represents the tangent line at the maximum value of volume strain (ε_v), and the tangent point indicates that the volume of red sandstone has been compressed to the greatest extent and started to shift from compression to expansion. The vertical coordinate of the tangent point is σ_{cd}. The purple dashed line connects the intersection of the brown dotted line of σ_{cd} and the axial strain (ε_a) curve to the origin, determining σ_{cc}. The pink dashed line connects the intersection of the brown dotted line of σ_{cd} and the lateral strain (ε_1) curve to the origin, determining σ_{ci}. The brown dotted line from top to bottom in Fig. 5 represents σ_{max}, σ_{cd}, σ_{ci}, and σ_{cc}. The specific results of CTTs under different σ_3 values are presented in Table 2 and Fig. 6.

The σ_{max}, σ_{cd}, σ_{ci} and σ_{cc} of sandstone showed an obvious linear relationship with σ_3. However, based on the slopes of the fitted lines, it was observed that σ_{cd} was predominantly influenced by σ_3, whereas σ_{ci} was the least affected and σ_{cc} was moderately affected. The values of σ_{cc}, σ_{ci} and σ_{cd} ranged in 13.75%−22.34%, 31.84%− 42.19%, and 63.85%−75.93% of σ_{max}, respectively. As shown in Fig. 6(c), σ_{cd}, σ_{ci} and σ_{cc} showed a decreasing trend from σ_3=0 to 2 MPa, indicating that the closure of natural cracks is promoted when σ_3 is small and new cracks generated faster. When σ_3 reached 8 MPa, σ_{cd}, σ_{ci} and σ_{cc} showed a significant upward trend with an increase in σ_3. This suggests that natural crack closure is inhibited but still occurs at a faster rate compared with that under a lower confinement state (σ_3<8 MPa). Moreover, the initiation and unstable growth rates were considerably slower when subjected to an applied confining pressure equal to or exceeding 8 MPa than below this threshold.

3.3 AE characteristics in CTTs

The variation of σ_3 in CTTs can influence the failure mode of the rock, which is reflected in the characteristics of AE parameters. AE can also be utilized to monitor the development of microcracks and the overall damage in sandstone under conventional triaxial stress. To thoroughly analyze differences in AE parameter characteristics, this study investigated typical AE data from three perspectives: AE hit, AE frequency, and AE amplitude–frequency characteristics. For obtaining repeated test data under identical conditions, only one comprehensive data file was selected as a representative for analysis.

3.3.1 Evolution law of AE hits

As shown in Fig. 7, in all CTTs, the number of AE hits was very low for a long period from the beginning of loading to rock failure, and several AE hits appeared within 50−150 s before the peak strength was reached. The time of appearance of several AE hits also differed under different σ_3 values. When σ_3 was smaller than 5 MPa, it started to appear within 50 s before the peak, and, when σ_3 was larger than 5 MPa, several AE hits appeared within 150 s before the peak strength. The onset of many AE hits can be regarded as a precursor to rock

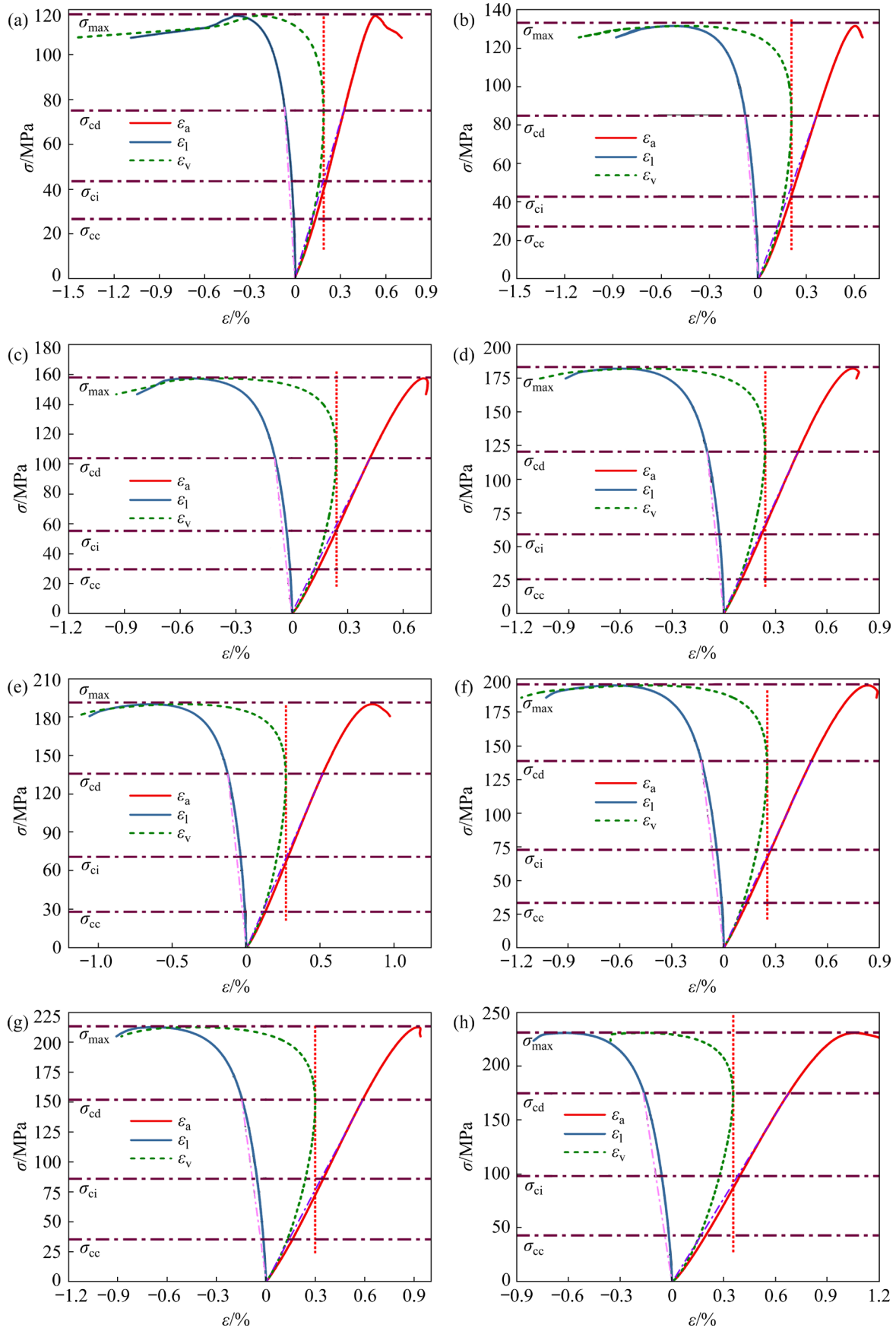

Fig. 5 Stress–strain curves in CTTs: (a) σ_3=0 MPa; (b) σ_3=2 MPa; (c) σ_3=5 MPa; (d) σ_3=8 MPa; (e) σ_3=10 MPa; (f) σ_3=12 MPa; (g) σ_3=15 MPa; (h) σ_3=20 MPa

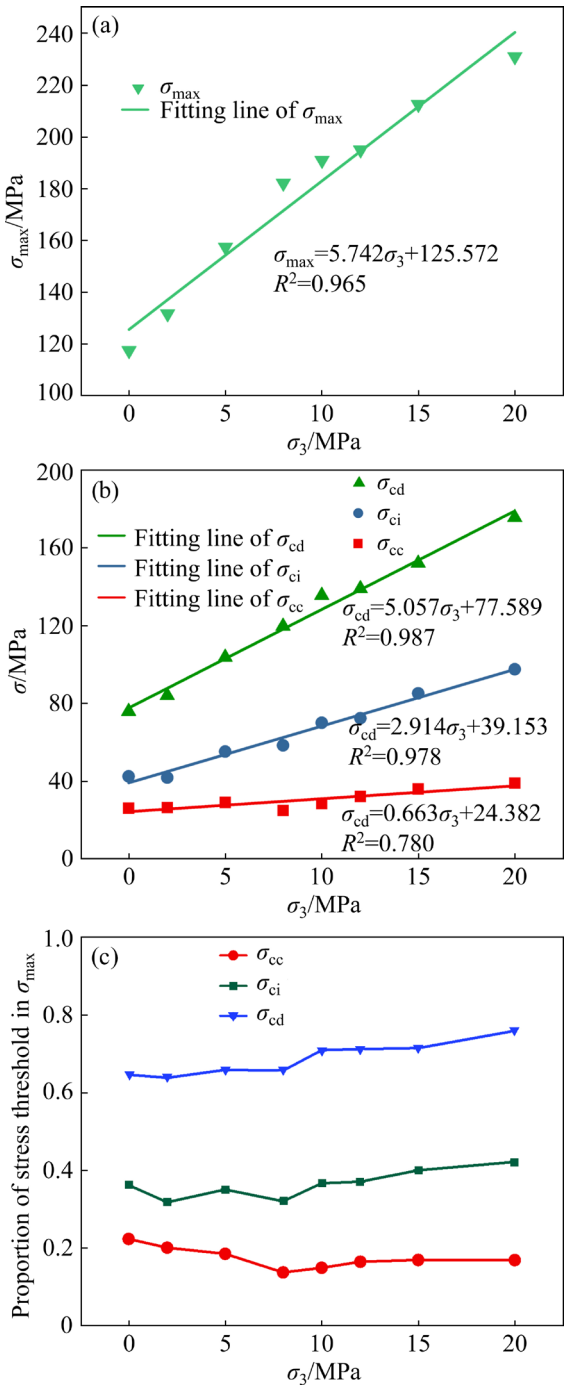

Fig. 6 Effects of confining pressure on different stress thresholds in CTTs: (a) σ_{max}; (b) σ_{cd}, σ_{ci} and σ_{cc}; (c) Proportion of σ_{cd}, σ_{ci} and σ_{cc} in σ_{max}

damage. Based on these observations, rock failure can be predicted 50 s in advance when σ_3 is small (≤5 MPa) and 150 s in advance when σ_3 is larger than 5 MPa. The cumulative number of AE hits generated throughout all CTTs ranged from 3000 to 4500, significantly higher than that generated under uniaxial compression, showing a slowly increasing trend with an increase in σ_3, as presented in Fig. 8 and Table 3.

Table 2 Stress thresholds of red sandstone under different stress states

σ_3/MPa	σ_{cc}/MPa	σ_{ci}/MPa	σ_{cd}/MPa	σ_{max}/MPa
0	26.23	42.51	75.85	117.39
2	26.49	41.88	84.03	131.62
5	29.17	55.23	103.67	157.39
8	25.04	58.41	119.63	182.12
10	28.55	70.05	135.44	190.93
12	32.19	72.35	138.84	194.97
15	36.04	85.14	151.96	212.57
20	39.08	97.46	175.40	231.02

3.3.2 Peak frequency distribution of AE signals

As shown in Fig. 9, the peak frequency of the AE signal was mainly distributed in the range of 0−100 kHz and 100−200 kHz, with a small amount of it in the range of 300−400 kHz. When σ_3 was low (between 0 and 5 MPa), the peak frequency in the range of 100−200 kHz rapidly increased as σ_3 increased. After σ_3 exceeded 5 MPa, the proportion of AE signals with a peak frequency of 300−400 kHz also increased as σ_3 continued to increase.

3.3.3 Relationship between amplitude and frequency of AE signals

The amplitude–frequency relationship of CTTs under different σ_3 values is shown in Fig. 10, where A is the AE amplitude, and N is the quantity of AE counts. Maintaining a loading rate of 0.10 mm/min for all CTTs inherently increased the likelihood of collision and extrusion between the sandstone and the pressure block, consequently leading to the generation of detectable signals monitored by the AE system. Hence, a meticulous analysis of AE amplitude–frequency characteristics is imperative. The evaluation of the efficacy of correlation analysis between amplitude and frequency for monitoring fatigue cracking and propagation across various materials, as substantiated by several scholars [34], was judiciously employed to scrutinize any aberrant AE signals.

In all conducted CTTs, a robust correlation between amplitude and frequency was observed, particularly in the logarithmic coordinate system, when σ_3 remained below 15 MPa. The linear

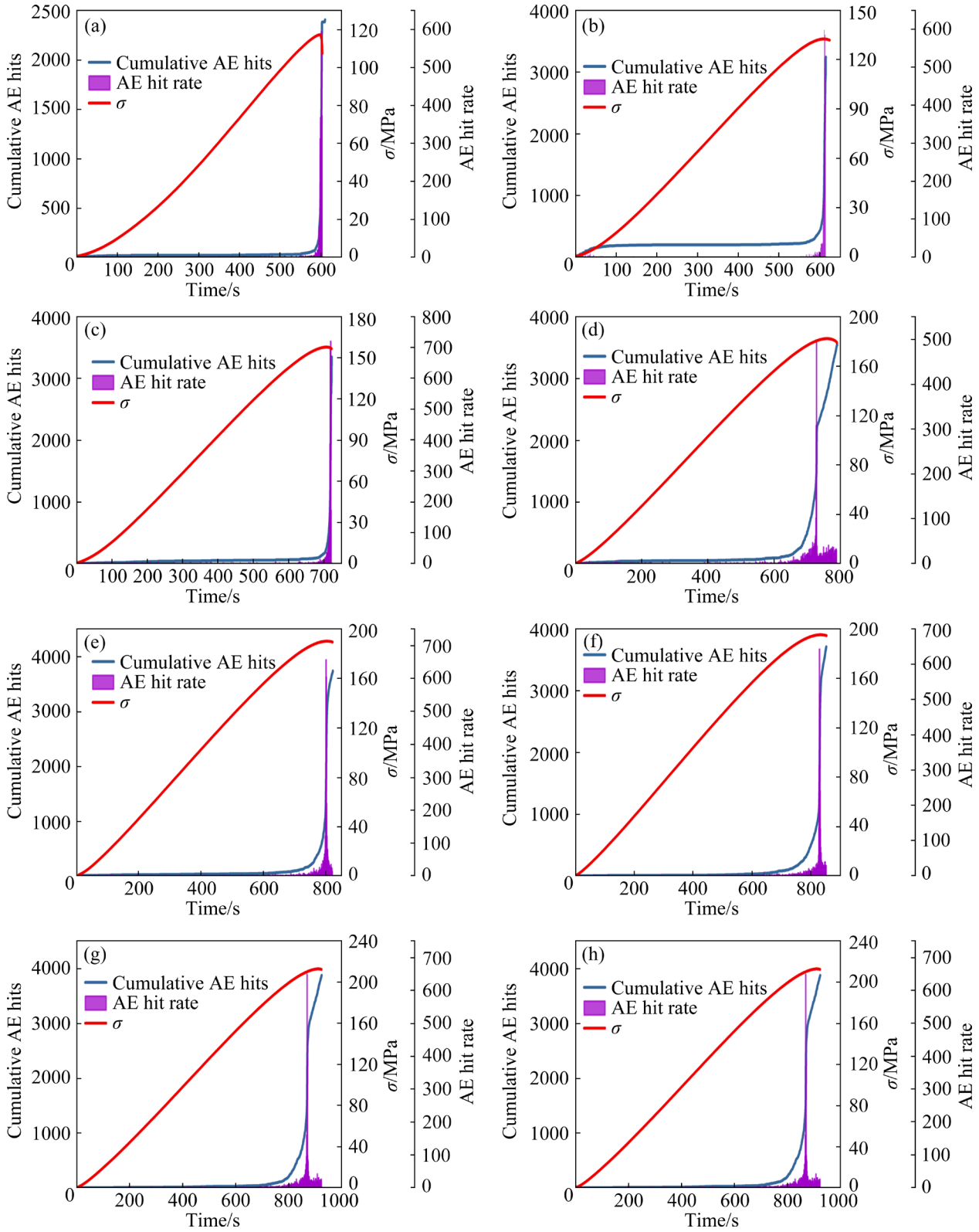

Fig. 7 Changes in AE hits in CTTs with time: (a) σ_3=0; (b) σ_3=2 MPa; (c) σ_3=5 MPa; (d) σ_3=8 MPa; (e) σ_3=10 MPa; (f) σ_3=12 MPa; (g) σ_3=15 MPa; (h) σ_3=20 MPa

relationship between amplitude and frequency exhibited a commendable goodness of fit at approximately 0.7, indicative of a heightened AE signal concentration and a concomitant reduction in noise signals. However, as the stress level σ_3 exceeded 15 MPa, an uptick in noise signals ensued,

potentially impinging upon the amplitude–frequency linear relationship, consequently diminishing the goodness of fit to approximately 0.6. This shift underscores the complex interplay between stress levels and AE signal characteristics, warranting further investigation to comprehensively elucidate the underlying mechanisms.

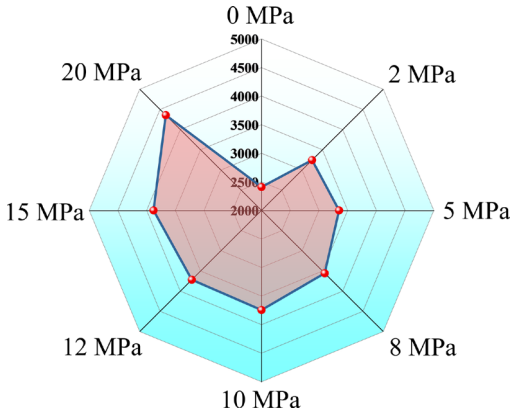

Fig. 8 Effect of σ_3 on cumulative number of AE hits in CTTs

Table 3 Cumulative AE hits in CTTs under different confining pressures

σ_3/MPa	Number of AE hits
0	2409
2	3245
5	3350
8	3557
10	3743
12	3716
15	3880
20	4359

4 Discussion

4.1 Parameters of shear strength in different tests

The cohesion force c reflects the ability of sandstone to withstand anisotropic unequal pressure, whereas the internal friction angle φ reflects the strength under the condition of anisotropic unequal

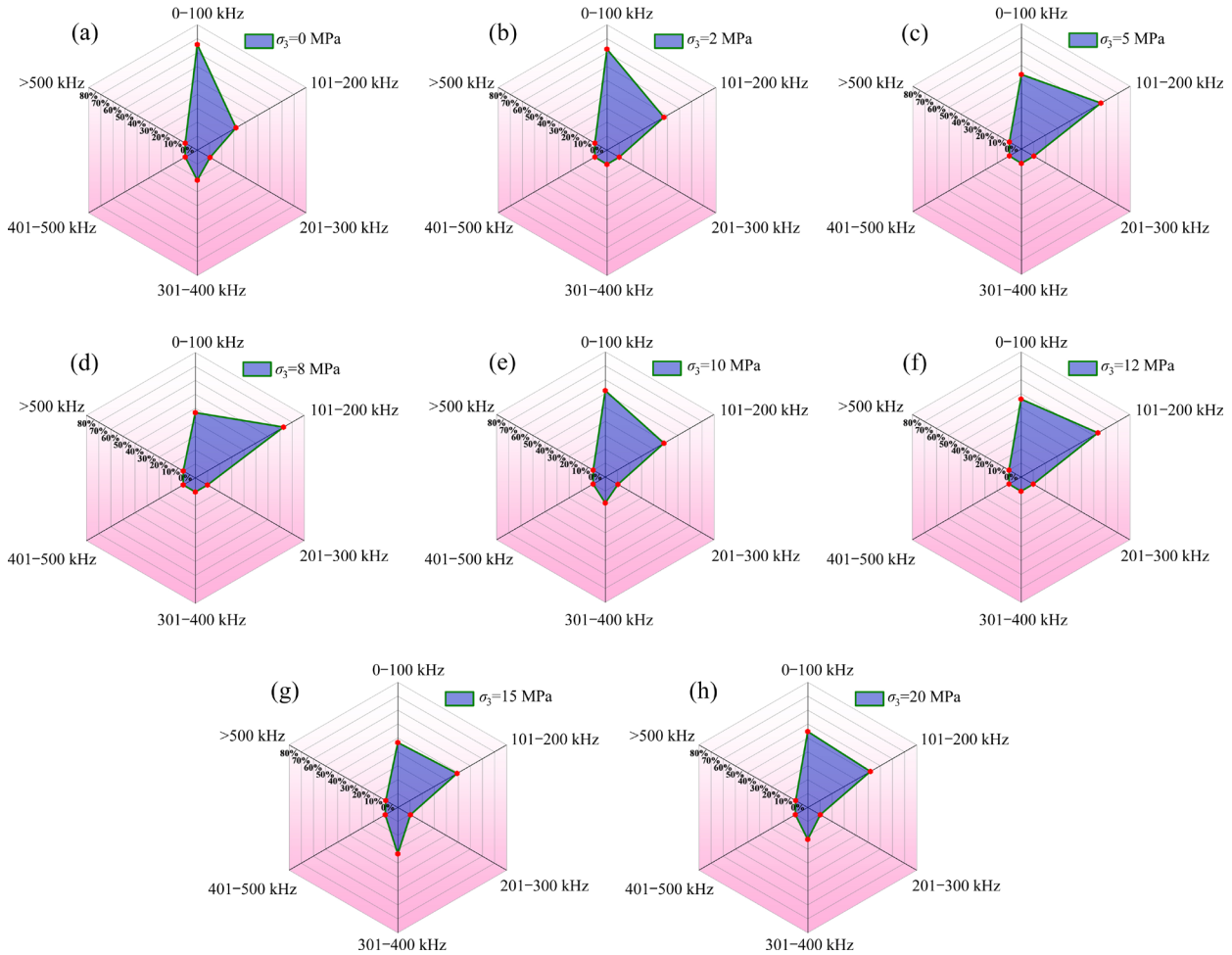

Fig. 9 Effects of σ_3 on AE peak frequency distribution

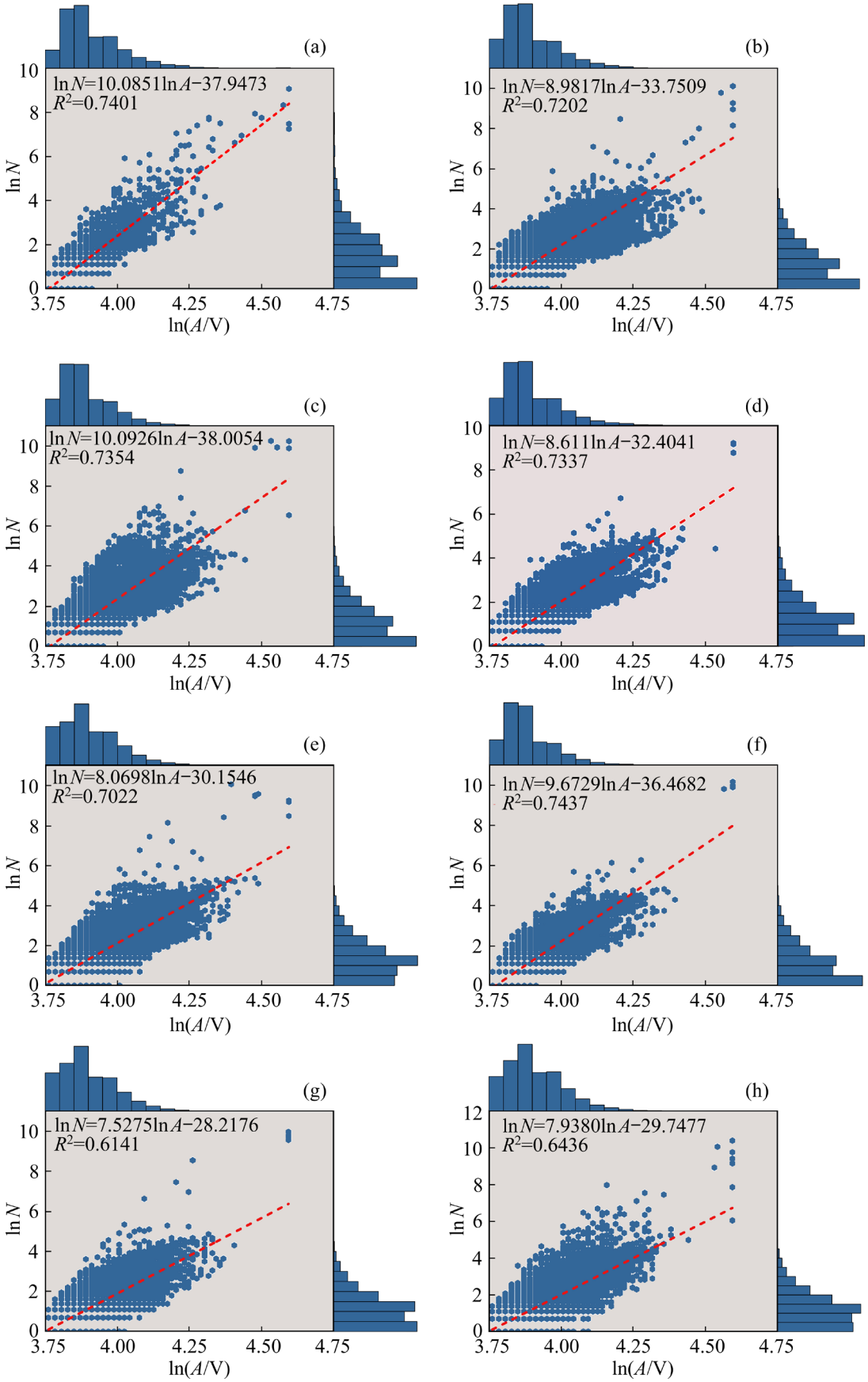

Fig. 10 Influence of σ_3 on amplitude–frequency relationship: (a) σ_3=0 MPa; (b) σ_3=2 MPa; (c) σ_3=5 MPa; (d) σ_3=8 MPa; (e) σ_3=10 MPa; (f) σ_3=12 MPa; (g) σ_3=15 MPa; (h) σ_3=20 MPa

Table 4 Shear strength parameters of red sandstone in CTTs under different σ_3 values

σ_3/MPa	c/MPa	φ/(°)
2, 5, 8, 10, 12, 15, 20	28.39	43.22
2, 5, 8, 10	21.68	49.69
5, 8, 10, 12	27.51	43.41
8, 10, 12, 15	35.03	38.82
10, 12, 15, 20	35.25	38.54

Table 5 Shear strength parameters of mechanical of red sandstone in VASTs under different α values

α/(°)	c/MPa	φ/(°)
45, 50, 60, 70	23.07	35.32
45, 50, 60	25.23	33.92
50, 60, 70	20.76	39.51

stress [35]. The determination of these two parameters is crucial for studying the stability of underground engineering projects. Generally, two common methods for determining the c and φ of rock are CTTs with different σ_3 values and VASTs with varying shear angles (α). In this study, a series of VASTs under different α values were conducted. Tables 4 and 5 present the evaluation results of c and φ determined in CTTs and VASTs, respectively. As σ_3 increased, c gradually increased, whereas φ gradually decreased in CTTs. The results of c obtained in CTTs and VAST ranged in 21.68−38.74 MPa and 20.76−25.23 MPa, respectively. Similarly, the results of φ obtained in CTTs and VASTs ranged in 38.54°−49.69° and 33.92°−39.51°, respectively.

The failure modes of red sandstone in VASTs with different shear angles are illustrated in Fig. 11, which shows that, as α increases, the sandstone failure tends to be simpler, with the predominance of shear failure. At α=45°, the damage resulting from compression became more pronounced. Hence, it is logical to opt for VASTs with shear angles ranging from 50° to 70° to calculate the shear strength parameters. By considering that the failure mode of rock in CTTs is not as distinctive as that under varied shear angles, c and φ can be calculated using the results of CTTs with σ_3 values ranging from 5 to 12 MPa.

4.2 Classification of tension–shear microcracks

Defining the proportion of tensile and shear cracks generated during the failure process of sandstone in a conventional triaxial stress state is important to determine the potential damage modes in underground engineering. It was proved that the generation of tensile cracks is accompanied by AE signals with large average frequency (f_a) and small a_r (a_r=t_r/A, t_r is the rise time) while the generation of shear cracks is accompanied by AE signals with small f_a and lager a_r. In the x−y coordinate system, a scatter plot of f_a−a_r is drawn with f_a as the vertical coordinate and a_r as the horizontal coordinate. Then, by determining a dividing line, the AE signal of the tension-shear crack can be discriminated. The dividing line (y=3x+75) [26] was applied. The points distributed above this dividing line represent the tensile cracks, whereas those below represent the shear cracks. The statistical analyses performed to classify the microcracks in CTTs are shown in Fig. 12.

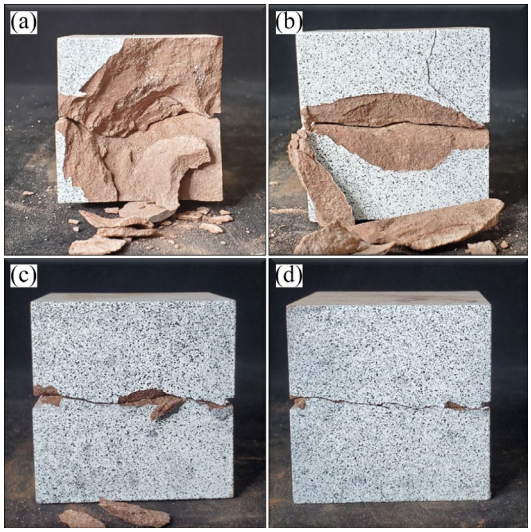

Fig. 11 Failure modes of sandstone in VASTs with α=45° (a), α=50° (b), α=60° (c), and α=70° (d)

In CTTs, the proportion of tensile cracks versus shear cracks with increasing σ_3 is listed in Table 6. Under the conventional triaxial state condition, σ_3 had a significant influence on the failure pattern of sandstone. Shear cracks play a significant role in the sandstone damage process. At σ_3=0−5 MPa, the proportion of shear cracks increased with an increase in σ_3, reaching its highest value of 84.55% at 5 MPa. This indicates that a small σ_3 value can promote shear damage, thereby increasing the proportion of transgranular cracks. When σ_3 was larger than 5 MPa, the proportion of tensile cracks increased with increase in σ_3. The proportion of shear cracks at σ_3=10 MPa was lower

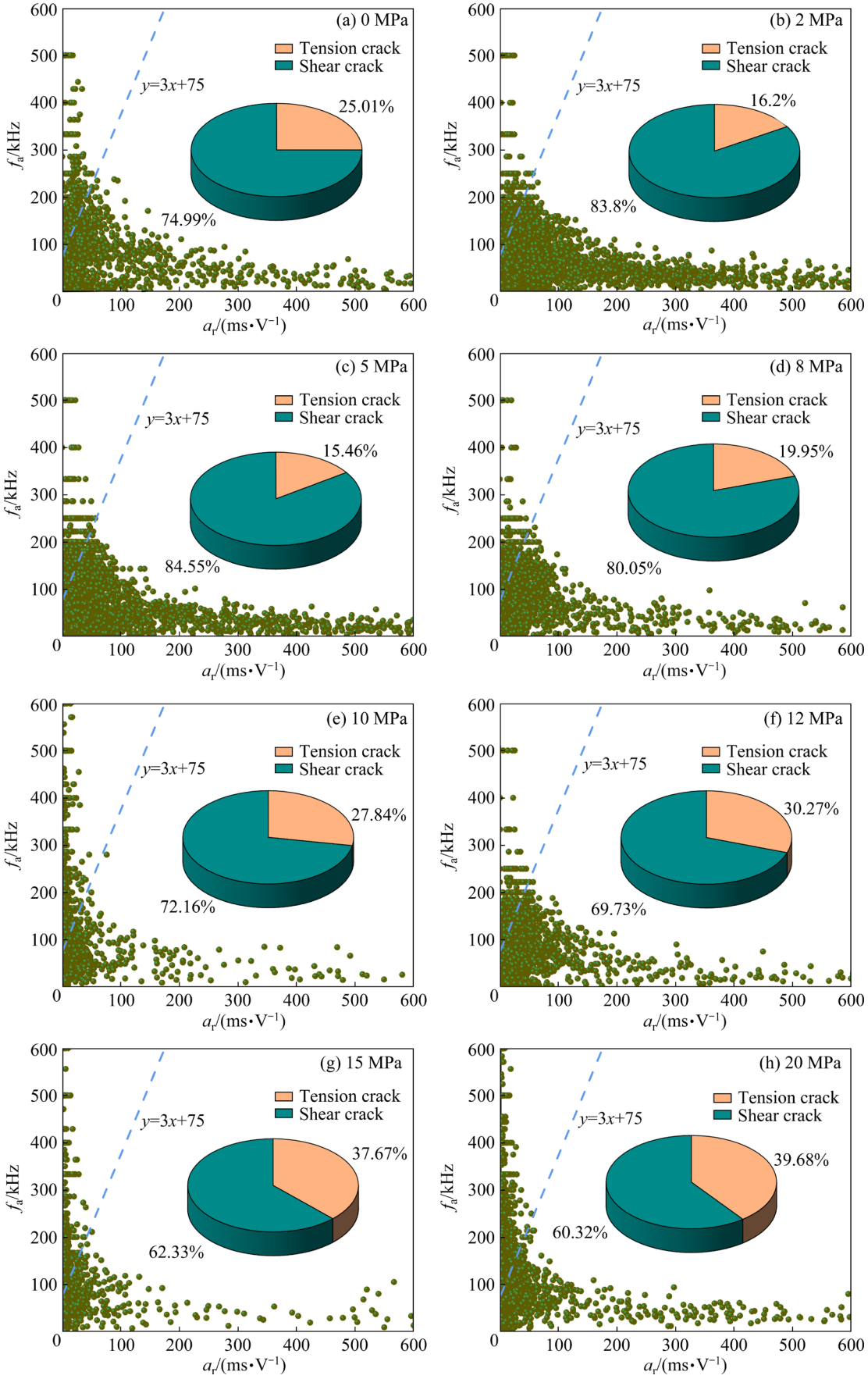

Fig. 12 Statistical charts of microcrack classification for sandstone in CTTs

Table 6 Proportion of tension and shear cracks of sandstone under different σ_3 values

σ_3/MPa	Proportion of tensile cracks/%	Proportion of shear cracks/%
0	25.01	74.99
2	16.22	83.78
5	15.45	84.55
8	19.95	80.05
10	27.84	72.16
12	30.27	69.73
15	37.67	62.33
20	39.68	60.32

than that in the uniaxial compression stress state. This indicates that, beyond a certain level of σ_3, the shear failure of sandstone is suppressed and tensile damage is promoted, thus increasing the proportion of intergranular cracks. When σ_3 ranged from 5 to 10 MPa, the change in the curve was more pronounced; however, when σ_3 ranged from 15 to 20 MPa, the change was smaller. Therefore, the larger the σ_3, the less pronounced the inhibitory effect on internal transgranular-shear breakage in the sandstone. According to the above analysis, when the surrounding rock of the underground oil and gas storage project is in the conventional triaxial stress state and σ_3 ranges from 5 to 10 MPa, special attention is needed on the change in the failure mode of the surrounding rock, focusing on its protection.

5 Conclusions

(1) The σ_{max} and all three stress thresholds, i.e., σ_{cd}, σ_{ci} and σ_{cc}, were positively correlated with σ_3. Furthermore, σ_{cd} was the most affected by σ_3, whereas σ_{cc} was the least affected. The activity of internal cracks accelerated when $\sigma_3 \leq 2$ MPa, whereas a large σ_3 value inhibited the closure of natural cracks and the generation and expansion of new cracks.

(2) The first sharp increase in the number of AE hits can be regarded as a precursor to damage. The peak frequencies of AE signals were primarily ranged in 0−100 kHz and 100−200 kHz, and an increase in σ_3 increased the peak frequency of AE signals.

(3) The c and φ values measured in the CTTs and VASTs differed. The results of φ and c measured in CTTs and VASTs were more accurate and reasonable when σ_3 and shear angle ranged in 5−12 MPa and 45°−70°, respectively.

(4) Shear cracks dominated the failure process of sandstone in CTTs. The proportion of tensile cracks increased and then decreased with an increase in σ_3. The shear failure of sandstone was promoted when $\sigma_3 \leq 5$ MPa and suppressed when $\sigma_3 \geq 10$ MPa. The suppression effect per unit of σ_3 was more pronounced when σ_3 ranged in 5−10 MPa and less apparent when σ_3 ranged in 15−20 MPa.

CRediT authorship contribution statement

Kun DU: Review, Supervision, Methodology, Investigation, Funding acquisition, Conceptualization; **Ming-hui LIU:** Writing – Original draft, Data curation, Formal analysis, Investigation, Validation, Software, Visualization, Funding acquisition; **Xue-feng LI:** Visualization, Data curation, Formal analysis, Investigation, Visualization; **Li-chang WANG:** Software, Project administration, Funding acquisition; **Jian ZHOU:** Supervision, Project administration; **Tao YANG:** Conceptualization; **Peng LI:** Data curation.

Declaration of competing interest

The authors declare that they have no known competing financial interests or personal relationships that could have appeared to influence the work reported in this paper.

Data availability

Data will be made available on request.

Acknowledgments

This research is partially supported by the National Natural Science Foundation of China (No. 52104112) and the Science and Technology Innovation Program of Hunan Province, China (Nos. 2021RC3007, 2020RC3090), as well as by the Fundamental Research Funds for the Central Universities of Central South University, China (No. 2024ZZTS0060).

References

[1] LUO Zhou-quan, WANG Wei, QIN Ya-guang, XIANG Jun. Early warning of rock mass instability based on multi-field coupling analysis and microseismic monitoring [J]. Transactions of Nonferrous Metals Society of China, 2019, 29(6): 1285−1293.

[2] XIA Kai-zong, CHEN Cong-xin, LIU Xuan-ting, LIU Xiu-min, YUAN Jia-hao, DANG Shuang. Assessing the stability of high-level pillars in deeply-buried metal mines stabilized using cemented backfill [J]. International Journal of Rock Mechanics and Mining Sciences, 2023, 170: 105489.

[3] ZHOU Zi-long, WU Zhi-bo, LI Xi-bing, LI Xiang, MA Chun-de. Mechanical behavior of red sandstone under cyclic point loading [J]. Transactions of Nonferrous Metals Society of China, 2015, 25(8): 2708−2717.

[4] WU Ting-yao, ZHOU Chuan-bo, JIANG Nan, XIA Yu-qing, ZHANG Yu-qi. Stability analysis for high-steep slope subjected to repeated blasting vibration [J]. Arabian Journal of Geosciences, 2020, 13: 828.

[5] TAO Ming, ZHAO Rui, ZHAO Hua-tao, WANG Yi-qing, CAO Wen-zhuo, WANG Shao-feng. Failure characteristics and energy distributions of surrounding rock in hard rock tunnels subjected to different three-dimensional stress conditions [J]. Transactions of Nonferrous Metals Society of China, 2023, 33(11): 3487−3502.

[6] ZHAO Yu-zhe, HUANG Lin-qi, LI Xi-bing, LI Chong-jin, CHEN Zheng-hong, CAO Zhi-wei. Failure modes and slabbing mechanisms of hard rock with different height-to-width ratios under uniaxial compression [J]. Transactions of Nonferrous Metals Society of China, 2022, 32(11): 3699−3713.

[7] LIU Yao, DENG Hong-wei. Study on permeability performance of cemented tailings backfill based on fractal characteristics of pore structure [J]. Construction and Building Materials, 2023, 365: 130035.

[8] YANG Sheng-qi, JING Hong-wen, WANG Shan-yong. Experimental investigation on the strength, deformability, failure behavior and acoustic emission locations of red sandstone under triaxial compression [J]. Rock Mechanics and Rock Engineering, 2012, 45: 583−606.

[9] ZHANG Bang-an, LI Xiao-ming, ZHANG Dong-ming. Study on mechanical and permeability characteristics of containing gas coal−rock under conventional triaxial compression [J]. Geotechnical and Geological Engineering, 2021, 39: 5775−5786.

[10] UH J, WATSON A T. Determining spatial distributions of permeability [J]. Transport in Porous Media, 2011, 86: 385−414.

[11] MARC S H. Evolution of mesozoic sandstone compositions, southern Junggar, northern Tarim, and western Turpan Basins, northwest China: A detrital record of the ancestral Tian Shan [J]. Journal of Sedimentary Research, 2000, 70: 520−532.

[12] AUZERAIS F M, DUNSMUIR J, FERRÉOL B B, MARTYS N, OLSON J, RAMAKRISHNAN T S, ROTHMAN D H, SCHWARTZ L M. Transport in sandstone: A study based on three dimensional microtomography [J]. Geophysical Research Letters, 1996, 23: 705−708.

[13] RODRIGUES M C N, TRZASKOS B, LOPES A P. Influence of deformation bands on sandstone porosity: A case study using three-dimensional microtomography [J]. Journal of Structural Geology, 2015, 72: 96−110.

[14] BAO Han, ZHAI Yong, LAN Heng-xing, ZHANG Ke-ke, QI Qun, YAN Chang-gen. Distribution characteristics and controlling factors of vertical joint spacing in sand-mud interbedded strata [J]. Journal of Structural Geology, 2019, 128: 103886.

[15] ZHANG He, SUN Qiang, LIU Lang, GE Zheng-long. Changes in glossiness, electrical properties and hardness of red sandstone after thermal treatment [J]. Journal of Applied Geophysics, 2020, 175: 104005.

[16] WANG Pin, YIN Tu-bing, LI Xi-bing, KONIETZKY H. Dynamic compressive strength and failure mechanisms of microwave damaged sandstone subjected to intermediate loading rate [J]. Transactions of Nonferrous Metals Society of China, 2022, 32(11): 3714−3730.

[17] WANG Peng, XU Jin-yu, LIU Shao-he, WANG Hao-yu. Dynamic mechanical properties and deterioration of red-sandstone subjected to repeated thermal shocks [J]. Engineering Geology, 2016, 212: 44−52.

[18] LI Jie-lin, ZHOU Ke-ping, LIU Wei-jie, DENG Hong-wei. NMR research on deterioration characteristics of microscopic structure of sandstones in freeze–thaw cycles [J]. Transactions of Nonferrous Metals Society of China, 2016, 26(11): 2997−3003.

[19] JEANPERT J, ISEPPI M, ADLER P M, GENTHON P, SEVIN B, THOVERT J F, DEWANDEL B, JOIN J L. Fracture controlled permeability of ultramafic basement aquifers: Inferences from the Koniambo massif, New Caledonia [J]. Engineering Geology, 2019, 256: 67−83.

[20] DAMJANAC B, FAIRHURST C. Evidence for a long-term strength threshold in crystalline rock [J]. Rock Mechanics and Rock Engineering, 2010, 43: 513−531.

[21] BRUNING T, KARAKUS M, NGUYEN G D, GOODCHILD D. Experimental study on the damage evolution of brittle rock under triaxial confinement with full circumferential strain control [J]. Rock Mechanics and Rock Engineering, 2018, 51: 3321−3341.

[22] DU Kun, SU Rui, TAO Ming, YANG Cheng-zhi, MOMENI A, WANG Shao-feng. Specimen shape and cross-section effects on the mechanical properties of rocks under uniaxial compressive stress [J]. Bulletin of Engineering Geology and the Environment, 2019, 78: 6061−6074.

[23] DU Kun, BI Rui-yang, SUN Yu, YANG Cheng-zhi, WANG Shan-yong, LI Gui-chen, WANG Shao-feng. Failure behaviors of granitic rocks induced by point/local loads under biaxial compression stress state [J]. Acta Geotechnica, 2023, 18: 4645−4669.

[24] DU Kun, LIU Ming-hui, YANG Cheng-zhi, TAO Ming, FENG Fu-kang, WANG Shao-feng. Mechanical and acoustic emission (AE) characteristics of rocks under biaxial confinements [J]. Applied Sciences, 2021, 11: 769−769.

[25] CHEN Dao-long, LIU Xi-ling, HE Wei, XIA Chang-gen, GONG Feng-qiang, LI Xi-bing, CAO Xin-ya. Effect of attenuation on amplitude distribution and *b* value in rock acoustic emission tests [J]. Geophysical Journal International, 2022, 229: 933−947.

[26] DU Kun, LI Xue-feng, TAO Ming, WANG Shao-feng. Experimental study on acoustic emission (AE) characteristics and crack classification during rock fracture in several basic lab tests [J]. International Journal of Rock Mechanics and Mining Sciences, 2020, 133: 104411.

[27] DU Kun, LI Xue-feng, WANG Shan-yong, TAO Ming, LI Gen, WANG Shao-feng. Compression-shear failure

properties and acoustic emission (AE) characteristics of rocks in variable angle shear and direct shear tests [J]. Measurement, 2021, 183: 109814.

[28] DU Kun, LI Xue-feng, YANG Cheng-zhi, ZHOU Jian, CHEN Shao-jie, MANOJ K. Experimental investigations on mechanical performance of rocks under fatigue loads and biaxial confinements [J]. Journal of Central South University, 2020, 27: 2985−2998.

[29] ZHAO Kui, YANG Dao-xue, GONG Cong, ZHUO Yu-long, WANG Xiao-jun, ZHONG Wen. Evaluation of internal microcrack evolution in red sandstone based on time–frequency domain characteristics of acoustic emission signals [J]. Construction and Building Materials, 2020, 260: 120435.

[30] LIU Ming-hui, LUO Xin-yao, BI Rui-yang, ZHOU Jian, DU Kun. Impacts of bedding angle and cementation type of bedding planes on mechanical behavior of thin-layer structured bedded rocks under uniaxial compression [J]. Geomechanics for Energy and the Environment, 2023, 35: 100473.

[31] ZHOU Y X, XIA K, LI X B, LI H B, MA G W, ZHAO J, ZHOU Z L, DAI F. Suggested methods for determining the dynamic strength parameters and mode-I fracture toughness of rock materials [J]. International Journal of Rock Mechanics and Mining Sciences, 2011, 49: 105−112.

[32] DU Kun, LI Xue-feng, SU Rui, TAO Ming, LV Shi-zhan, LUO Jia, ZHOU Jian. Shape ratio effects on the mechanical characteristics of rectangular prism rocks and isolated pillars under uniaxial compression [J]. International Journal of Mining Science and Technology, 2022, 32: 347−362.

[33] NICKSIAR M, MARTIN C D. Crack initiation stress in low porosity crystalline and sedimentary rocks [J]. Engineering Geology, 2013, 154: 64−76.

[34] LIU Xi-ling, LIU Zhou, LI Xi-bing, GONG Feng-qiang, DU Kun. Experimental study on the effect of strain rate on rock acoustic emission characteristics [J]. International Journal of Rock Mechanics and Mining Sciences, 2020, 133: 104420.

[35] ZHU De-fu, YU Biao-biao, WANG De-yu, ZHANG Yu-jiang. Fusion of finite element and machine learning methods to predict rock shear strength parameters [J]. Journal of Geophysics and Engineering, 2024, 21: 1183−1193.

硬质红砂岩在结合声发射的常规三轴压缩试验中的力学性能

杜 坤[1]，刘明晖[1]，李雪锋[1]，王李昌[2]，周 健[1]，杨 涛[3]，李 鹏[4]

1. 中南大学 资源与安全工程学院，长沙 410083；
2. 中南大学 地球科学与信息物理学院，长沙 410083；
3. 华北科技学院 矿山安全学院，廊坊 065201；
4. 中南勘测设计研究院有限公司，长沙 410014

摘 要：设计了一系列结合声发射的常规三轴压缩试验(AE-CTTs)评估一种硬质红砂岩的力学性能。在常规三轴应力条件下，砂岩的裂纹闭合应力、裂纹起裂应力和损伤应力分别占峰值强度的 13.75%~22.34%、31.84%~42.19%和 63.85%~75.93%。声发射参数可以反映围压(σ_3)对微裂纹扩展的影响，σ_3=5 MPa 是影响砂岩声发射撞击数激增时间点和最终破坏前声发射信号峰值频率分布范围的阈值。声发射特性分析表明，剪切裂纹在砂岩常规三轴压缩破坏过程中占主导地位，占裂纹总数的 60%~85%，且较小的围压会促进剪切破坏，而较大的围压则会抑制剪切破坏。此外，确定了在常规三轴压缩试验和变角剪切试验中用于准确计算内聚力和内摩擦角合适的数据集选取范围。

关键词：红砂岩；力学参数；应力阈值；声发射特征；内摩擦角；内聚力

(Edited by Xiang-qun LI)